



The role of carbon nanotube in zinc stannate photocatalytic performance improvement: Experimental and kinetic evidences

M.S. Seyed Dorraji ^{a,*}, A.R. Amani-Ghadim ^{b,*}, M.H. Rasoulifard ^a, S. Taherkhani ^a, H. Daneshvar ^a

^a Applied Chemistry Research Laboratory, Department of Chemistry, Faculty of Science, University of Zanjan, Zanjan, Iran

^b Department of Chemistry, Faculty of Science, Azarbaijan Shahid Madani University, P.O. Box 83714-161, Tabriz, Iran



ARTICLE INFO

Article history:

Received 11 October 2016

Received in revised form

19 December 2016

Accepted 1 January 2017

Available online 3 January 2017

Keywords:

MWCNTs

Nanocomposite

Kinetic modeling

Photocatalytic mechanism

ABSTRACT

The $\text{Zn}_2\text{SnO}_4/\text{MWCNTs}$ (ZSC) nanocomposite was synthesized by a facile two-step process. The as-prepared nanocomposite was characterized by Powder X-ray diffraction, scanning electron microscopy, Transition electron microscopy, UV-vis diffuse reflectance spectroscopy and photoluminescence spectra analysis. The ZSC nanocomposite exhibits much higher photocatalytic activity (94% removal in 120 min) in comparison with bare Zinc stannate (ZS) (17% removal in 120 min) under UV-A irradiation, toward degradation of Basic Red 46. The role of the MWCNTs on the observed enhancement in photocatalytic activity was revealed by investigating the effect of radical scavengers on degradation efficiency. The addition of BQ had no effect on photocatalytic efficiency and *t*-butanol decreased the photocatalytic activity to some extent. However, the addition of iodide ion, as a hole scavenger, inhibited completely the photocatalytic degradation of BR46, indicating that the degradation of the BR46 occurs mostly by direct oxidation on photogenerated holes. Based on the results of experiments, DRS and PL spectra, two possible mechanisms were proposed. Moreover, a new kinetic model was developed based on the intrinsic elementary reactions and the proposed mechanism. The correlation coefficient (R^2) and root-mean-square-error (RMSE) of 0.990 and 7.12×10^{-4} indicates the good agreement between the calculated apparent rate constants and experimental ones.

© 2017 Elsevier B.V. All rights reserved.

1. Introduction

Over the past two decades, the fascinating mechanical, chemical and electrical properties of Carbon Nanotubes—the one dimensional form of sp^2 -hybridized carbon- [1], have open a new window toward solving the well-known issues in different research areas including, nanoelectronics [2], polymer science [3], electrochemical energy storage devices [4], catalysis and photocatalysis [5].

Regarding to the domain of photocatalysis, the major challenges are to increase the visible light absorption capability, decrease the recombination rate of photo-induced electron-hole pairs and preventing the aggregation of catalyst particles [6]. The unique features of CNTs namely, conductivity and electron accepting and transporting properties, ability to respond to visible light and high specific surface area, make them capable to overcome these prob-

lems [7–10]. Hence, enormous interest have been promoted in synthesize CNT-semiconductor nanocomposites and great amount of literature have been reported the enhanced photoactivity of these nanocomposites [10–19].

The enhancement of photocatalytic performance of studied nanocomposites can be explained by different mechanisms. It has been reported that CNTs can act as a macromolecule photosensitizers, which enhanced the visible light absorption capability by photoexcitation of electrons from the ground state of CNTs to its excited state. The excited electrons can then injected into the conduction band of semiconductor, allowing the formation of superoxide radicals [16,17]. Another different mechanism, is introducing a new carbon energy level into the semiconductor band gap and thereby extending the light absorption of composite to longer wavelengths [18]. The other proposed mechanism is attributed to the fact that CNTs have large electron-storage capacity, hence the photo-excited electrons can be transferred from the space-charge region of semiconductor into CNTs upon illumination, resulting in prolongation of life span of photoexcited electron-hole pairs [8,19]. CNTs can also make it possible to obtain a higher surface area and

* Corresponding authors.

E-mail addresses: dorraji@znu.ac.ir, saeed.dorraji@yahoo.com (M.S. Seyed Dorraji), a.r.amani@yahoo.com, amani.gh@azaruniv.edu (A.R. Amani-Ghadim).

play a role as a dispersing template to prevent the agglomeration of catalyst particles [12,20].

Even though the photocatalytic activity of CNTs-semiconductor nanocomposite have been widely investigated, proposing a more detailed mechanism for understanding the photocatalytic processes in these systems is still a major challenge. To achieve this purpose, modeling a photocatalytic process can significantly enhance the understanding of the responsible mechanism of photoactivity [21]. The kinetic study plays an important role in discovering the reaction mechanism and estimating the influences of different operation parameters [22]. Hence, modeling of processes based on the kinetic studies is one of the best modeling methods, since it is based on correct understanding of happened reactions in the process [23].

The previous studies mostly focused on CNTs-binary oxide semiconductor nanocomposites (e.g., TiO₂, ZnO, ZnS, and CdS) [24–28]. Nevertheless, in comparison with simple binary oxides, ternary oxides have more ability to tune the chemical and physical properties by altering the compositions [29]. Zinc stannate (Zn₂SnO₄), as one of the most important ternary oxides, have been studied in wide range of applications such as anode material for dye sensitized solar cells (DSCs) [30], Li⁺ batteries [31] and photocatalysts for pollution decomposition [32,33]. However the high charge separation rate induced by surface oxygen-vacancies and high chemical stability, make ZS a good candidate for photocatalysis [22,34], but, the high band gap energy of 3.0–3.9 eV, hinder its applicability in photocatalytic processes [35].

Herein, we have synthesized Zn₂SnO₄/MWCNTs nanocomposite via a simple two-step process and the photocatalytic performance of the prepared sample was investigate by photodegradation of Basic Red 46 as a model organic pollutant. As the photocatalytic activity is closely related to the type and amount of the produced active species, a series of experiments were conducted in the presence of appropriate scavengers. Moreover, in order to dig out the more detailed mechanism of photocatalytic performance of CNT-semiconductor nanocomposite, a kinetic model was developed based on the intrinsic elementary reactions and the proposed mechanism and the adequacy of the proposed model to fit the experimental results was further discussed.

2. Experimental

2.1. Materials

Multi-walled carbon nanotubes (MWCNTs, 20 nm in diameter and 30 μm in length, purity >95 wt%) were purchased from Neutrino Co, Iran. The stannic chloride pentahydrate (SnCl₄·5H₂O) and zinc nitrate [Zn(NO₃)₂] was purchased from Sigma-Aldrich CO. NaOH and BR46 were obtained from Merck (Germany).

2.2. Synthesis

In order to synthesize ZCS nanocomposie, 0.05 g MWCNTs was dispersed into deionized (DI) water by sonication for 15 min. SnCl₄·5H₂O (3 mmol) and Zn(NO₃)₂ (3 mmol) were dissolved in 20 mL of double distilled water separately to give two transparent solutions. Afterward, 20 mL NaOH (1 M) was added dropwise into the tin chloride dihydrate solution and then the resultant solution was added drop by drop into mentioned MWCNT solution. After the addition was completed, zinc nitrate solution was added drop by drop into above mixed solution under vigorous stirring at room temperature until the formation of grey precipitate of the hybrid complex. Finally, the grey precipitate was transferred into a 100 mL Teflon-lined stainless. The autoclave was sealed and maintained in a furnace at 220 °C for 48 h. The autoclave was cooled naturally to

room temperature. The obtained precipitate was washed several times in double distilled water and absolute ethanol by repeated centrifugation and ultrasonication. Finally, the product was dried in an oven at 80 °C for 20 h.

2.3. Characterization

The structure, phase composition and real size of prepared nanocomposites were determined by Powder XRD investigations using Siemens X-ray diffraction ((D5000, Germany), with Cu K α radiation(1.54065 Å and $\theta=5\text{--}75^\circ$)). The surface morphology was analyzed by TEM (JEOL, JEM 2200) and FESEM (MIRA3 FEG-SEM, Tescan). DRS and PL spectra were obtained with a Perkin-Elmer, Lambda 25 and JASCO FP-6200, respectively

2.4. Procedure

The photocatalytic activity of ZSC nanocomposite was evaluated by the degradation of Basic Red 46 as a dye pollutant. In a typical process, 140 mg/L of catalyst was suspended into aqueous solution of BR43 with a known initial concentration. The suspended solution was irradiated by 390 nm emmiting UV-LED with a maximum power of 150 W. At specific time intervals, suspension was sampled and centrifuged to remove the catalyst particles. The pH of solution kept constant at 9. The light intensity and initial dye concentration were kept constant at 36 W/m² and 14 mg/L respectively, except for investigating the effect of these two factors on photocatalytic efficiency. Photocatalytic activity experiments using different radical scavengers were performed similar to the above procedure but in the presence of 1 mM different radical scavenger.

3. Results and discussion

3.1. Characterization of the ZSC nanocomposite

The crystal structure and phase composition of ZSC nanocomposite were determined by X-ray powder diffraction. Fig. 1 shows the XRD pattern of the as-prepared sample. The reflection peaks of (111), (220), (311), (220), (400), (422), (511) and (440) are attributed to the spinel structure of Zn₂SnO₄ [30,32]. The small marked residual peak at around $2\theta=26^\circ$ can be assigned to 002 plane of MWCNTs [36,37]. High crystallinity of the prepared Zn₂SnO₄/MWCNT is confirmed by the strong, narrow and intense reflection peaks in the XRD. Additionally, no diffraction peaks of SnO₂ were observed confirming the phase purity of the prepared nanocomposite.

The morphology of Zn₂SnO₄/MWCNT nanocomposite was investigated using scanning electron microscopy (Fig. 2). SEM images show the distribution of Zinc Stannate nanoplates across 1D CNTs. Fig. 2b also confirms that Zn₂SnO₄ have been synthesized in nanoplates form. TEM micrograph of Zn₂SnO₄/MWCNTs nanocomposite indicates the presence of Zn₂SnO₄ nanoplates on the walls of MWCNTs. The diameter of the MWCNTs is about 20 nm and the thickness is about 7 nm.

The optical absorption properties of prepared ZS and ZSC nanocomposite are investigated by diffuse reflectance spectroscopy (Fig. 3a). UV-vis absorption spectra revealed that the ZS could only absorb wavelengths shorter than 340 nm, which is attributed to its inartistic band gap. It is obvious in ZS UV-vis spectrum that the addition of the CNTs to ZS yields to shift in adsorption edge toward the longer wavelengths (400 nm). The optical band gap energies for prepared photocatalysts were determined by Tauc-Mott plot (TM) derived from following Eq. [38]:

$$(AE)^{1/m} = B(E - E_g) \quad (1)$$

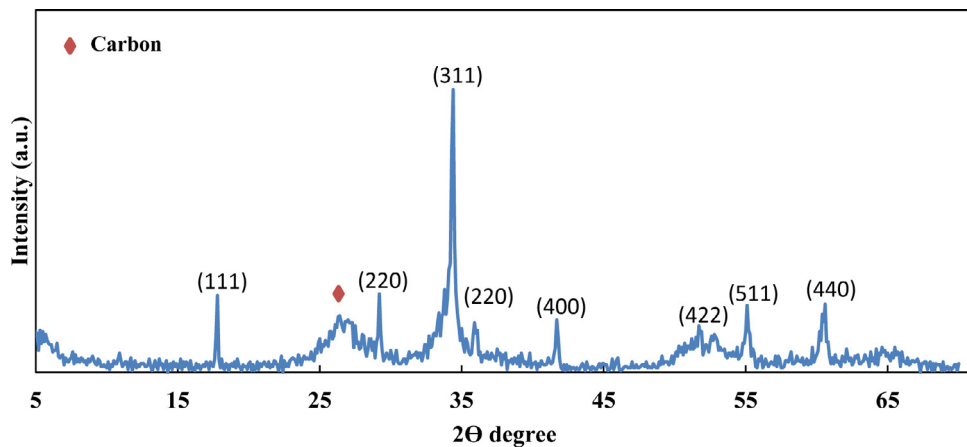


Fig. 1. XRD pattern of ZSC nanocomposite.

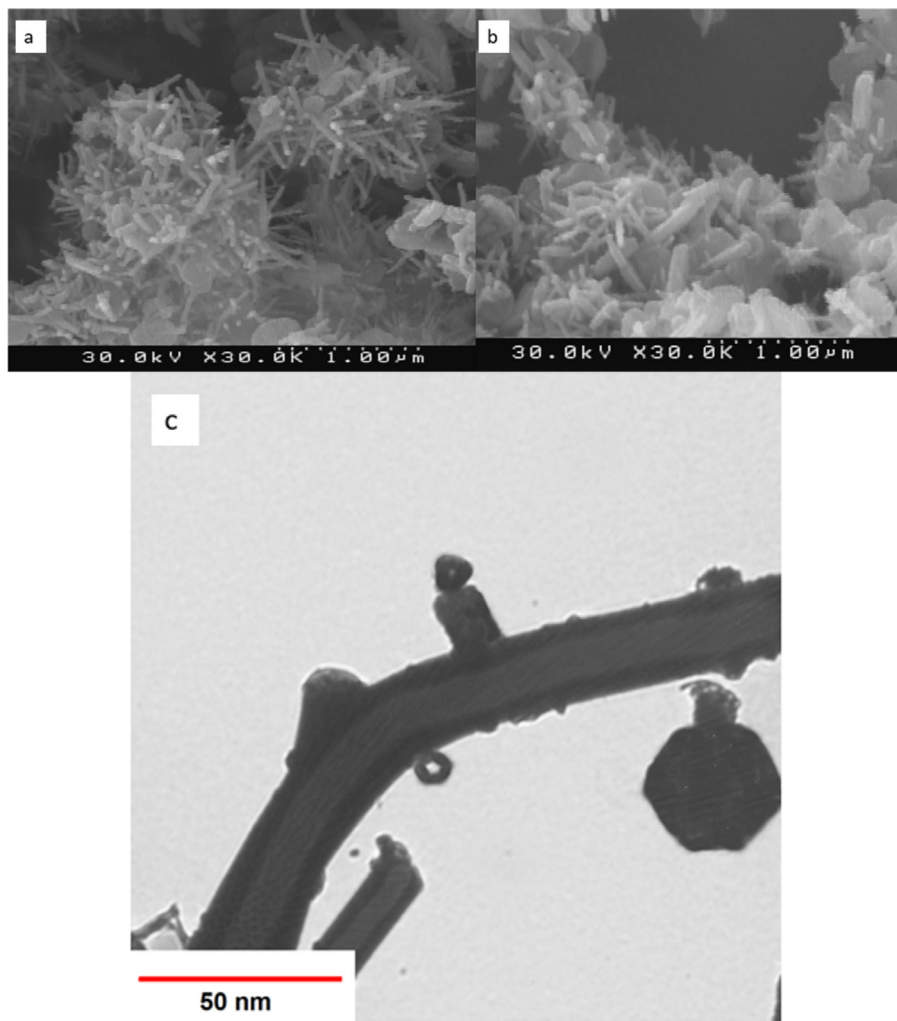


Fig. 2. SEM (a and b) and TEM (c) of ZSC nanocomposite.

In this Eq., A represents the UV-vis absorbance, B is proportional constant and E is the photon energy ($h\nu$). The exponent m value is attributed the type of the electron transitions which is the inherent property of the semiconductor. Its value equals to $1/2$, $3/2$, 2 and 3 for direct allowed, direct forbidden, indirect allowed and indirect forbidden transitions, respectively. This means that to assess the band gap energy from DRS data, the transition type must be spec-

ified. Alpuche-Aviles and Wu proposed direct forbidden transition based on the best fitting of experimental data on various transition states [39]. We also plotted the TM for the prepared ZS and ZSC by considering the direct forbidden transition (Fig. 3b). The band gap of ZS and ZSC was determined to be 3.7 and 3.15 eV respectively by extrapolating of the linear section of the TM plot to $(Ah\nu)=0$ to intercept the $h\nu$ axis.

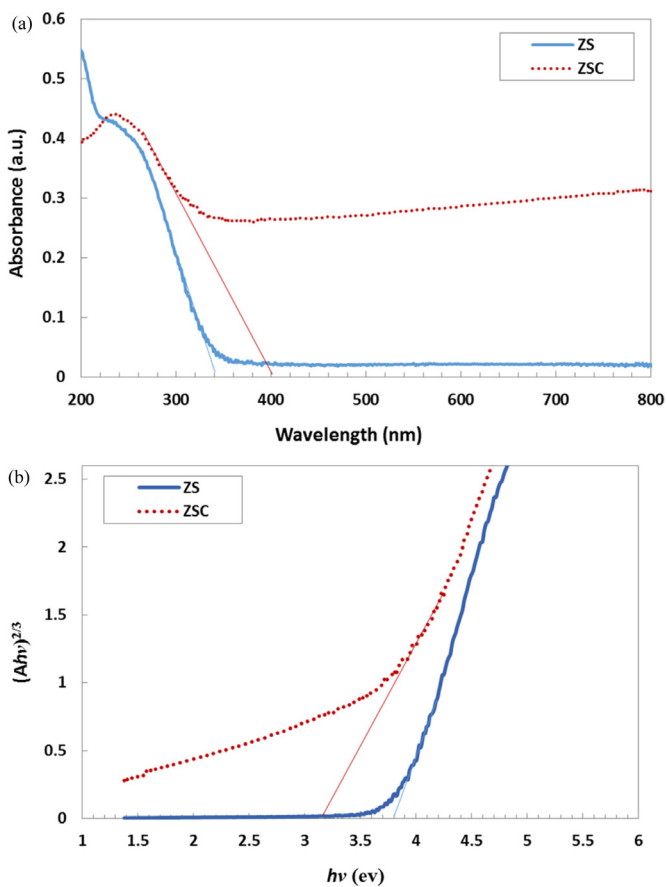


Fig. 3. (a) UV-vis adsorption spectrum of synthesized ZS and ZSC, and (b) corresponding TM plot of vs. energy of photon.

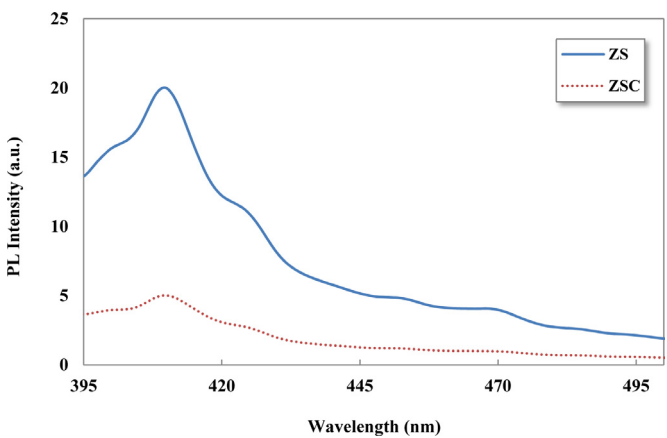


Fig. 4. PL spectra of synthesized ZS and ZSC with 380 excitation wavelength.

Photoluminescence spectra (PL) of ZS and ZSC were measured to reveal the effective role of MWCNT in separation of photoinduced charge carriers. The PL spectra of ZS and ZSC are shown in Fig. 4. The PL emission intensity of ZSC nanocomposite is considerably weaker than ZS implying the notable suppression of electron-hole recombination. This result could be attributed to electron transfer from ZS to carbon nanotube.

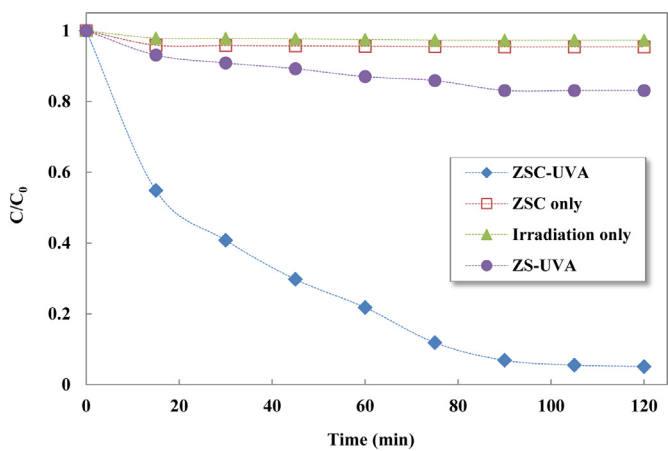


Fig. 5. Effective photocatalytic performance of prepared ZSC under UV-A LED irradiation. Experimental conditions: $[BR46] = 14 \text{ mg/L}$, Catalyst dosage = 140 mg/L , pH = 9 and L.I. = 36 W/m^2 .

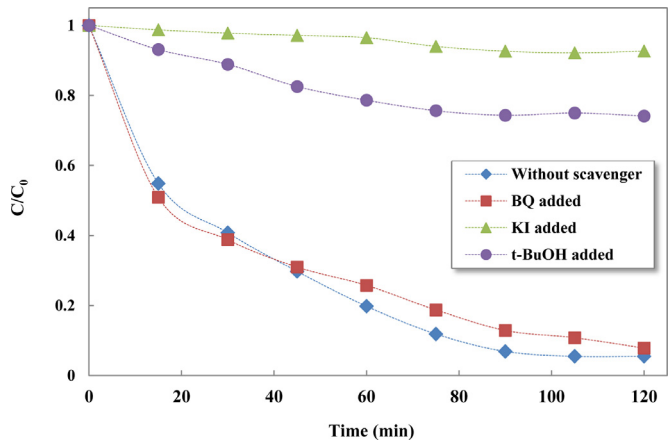


Fig. 6. Effect of scavengers on photocatalytic performance of ZSC in degradation of the BR46 under UV-A LED irradiation. Experimental conditions: $[BR46] = 14 \text{ mg/L}$, Catalyst dosage = 140 mg/L , pH = 9 and L.I. = 36 W/m^2 . [scavenger] = 1 mM .

3.2. Photocatalytic activity of zinc stannate/MWCNT nanocomposite

To evaluate the photocatalytic activity of prepared ZSC nanocomposite, a series of experiments were conducted without light irradiation or catalyst and in the presence of catalyst under UV-A LED irradiation (Fig. 5). After 120 min of experiments, 94.5% of initial dye concentration was destroyed in photocatalytic process whereas the removal efficiency was less than 5% in absence of light irradiation or catalyst. The negligible degradation efficiency in the absence of light or catalyst reveals that the considerable degradation of dye by ZSC under UVA irradiation is individually achieved by photocatalytic reaction of the prepared nanocomposite. Moreover, the degradation efficiency of dye in the presence of zinc stannate was about 17% after 120 min under UV-A –LED irradiation. Accordingly, in comparison with ZS, ZSC possesses considerable photocatalytic activity under longer wavelengths irradiation because of a shift of its absorption edge to higher wavelength.

To reveal the responsible mechanism for photocatalytic degradation of BR46 on the prepared ZSC, a series of experiments has been conducted by adding the various scavengers. As shown in Fig. 6, the addition of benzoquinone (BQ), as superoxide anion radical (O_2^-) scavenger, has no effect on photocatalytic degradation of BR46. In contrast, when the hydroxyl radical scavenger, *tert*-butyl alcohol (t-BuOH), was added to the BR46 solution, the

Table 1

Elementary reactions involved in photocatalytic degradation of BR46 on ZSC.

Elementary reaction	Reaction rate equations	No.
$ZSC + h\nu \xrightarrow{\lambda=390\text{nm}} ZSC(h^+ + e^-)$	$r_{irr} = k_{irr} I$	R1
$ZSC(h^+ + e^-) \rightarrow h\nu \text{ or heat}$	$r_{recomb} = k_{recomb} [h^+] [e^-]$ $\Rightarrow [BR46]_{ads} = K_{BR46} [BR46]_{aq}$	R2
$BR46_{(aq)} \leftrightarrow BR46_{(ads)}$		R3
$H_2O_{(aq)} \leftrightarrow H_2O_{(ads)}$		R4
$OH^-_{(aq)} \leftrightarrow OH^-_{(ads)}$		R5
$ZSC(h^+) + H_2O_{ads} \rightarrow ZSC(\cdot OH)_{ads} + H^+$	$r_{H_2O} = k_{H_2O} [h^+] [H_2O]_{ads}$	R6
$ZSC(h^+) + OH^-_{ads} \rightarrow ZSC(\cdot OH)_{ads}$	$r_{OH^-} = k_{OH^-} [h^+] [OH^-]_{ads}$	R7
$ZSC(h^+) + BR46_{(ads)} \rightarrow ZSC + Int_{ads}$	$r_{BR46} = k_{BR46} [h^+] [BR46]_{ads}$	R8
$ZSC(h^+) + Int_{ads} \rightarrow ZSC + CO_2 + H_2O$	$r_{Int} = k_{Int} [h^+] [Int]_{ads}$	R9
$ZSC(\cdot OH)_{ads} + BR46_{(ads)} \rightarrow Int$	$r_{\cdot OH, BR46} = k_{\cdot OH, BR46} [\cdot OH]_{ads} [BR46]_{ads}$	R10
$ZSC(\cdot OH)_{ads} + Int \rightarrow CO_2 + H_2O$	$r_{\cdot OH, Int} = k_{\cdot OH, Int} [\cdot OH]_{ads} [Int]_{ads}$	R11
$ZSC(\cdot OH)_{ads} \rightarrow ZSC(OH^-)_{ads} + h^+$	$r_{inact} = k_{inact} [\cdot OH]_{ads}$	R12

degradation efficiency decreased remarkably. In the presence of the t-BuOH, the degradation efficiency of BR46 after 120 min of UV-A irradiation was 25.87%. The unexpected result was obtained when photocatalytic degradation of the BR46 by ZSC was carried out in the presence of the iodide anion as a holes scavenger. The hole scavenger inhibited completely the photocatalytic degradation of BR46. So, it could be concluded that the photocatalytic degradation of the BR46 occurs via direct oxidation on photogenerated holes and hydroxyl radicals.

Summing up the results of experiments carried out with adding the various scavengers and DRS spectra, we could propose two reasonable mechanisms to explain the role of the CNTs in photocatalytic activity of ZSC nanocomposite. Although the band structure of MWCNTs depends on different factors such as diameter and chirality of nanotubes, generally the carbon nanotubes are known as semiconductors with narrow band gap energy [40]. The irradiated photons are absorbed by carbon nanotubes generating electron-hole pairs on the CNT. The photogenerated electrons transfer to conduction band of the ZS and the positively charged CNT remove an electron from the VB of the ZS. The formed holes on the VB of ZS react with dye and/or water molecules to generate the hydroxyl radicals. In the second mechanism, it could be reasonably assumed that the extension of light absorption to longer wavelengths is conducted by carbon-oxygen-ZS band. In this case, the electrons in VB of the ZS are excited to carbon nanotube and shuttled freely along the conductive network of the CNT, similar to what happens in surface carbon doping. The longer lived holes have sufficient opportunity for trapping by dye and water molecules.

The enhancement of the photocatalytic activity of semiconductor/CNT nanocomposite could be explained by other mechanisms reported in literature [17]. The first mechanism involves the excitation of an electron from the valence band (VB) of ZS to its conduction band followed by the transformation of the electrons into CNTs. Herein, the CNT acts as the electron reservoir and the remaining holes in the ZS participate in oxidation reactions. In our work, the occurrence of this mechanism is unlikely because the energy of emitted photons from the UVA LED is not enough to provide the

state followed by the electron injection to conduction band of the ZS. The electrons in the CB of the ZS reduce the adsorbed molecular oxygen and generate superoxide anion radical which is strong oxidizing agent. In this pathway superoxide anion radical is the main destructive agent for degradation of organic pollutants. The results of experiments carried out with adding BQ do not confirm the photosensitizer role of CNT in photocatalytic degradation of the BR46 by ZSC.

As the results of experiments carried out by scavengers revealed, the photocatalytic degradation of the BR46 on ZSC is occurred via direct oxidation by photogenerated holes and indirect oxidation by hydroxyl radicals. A sequence of elementary reactions is given in Table 1. It is assumed that the organic molecules are degraded by holes and/or reactive radicals on the surface of photocatalyst. Accordingly, the linear BR46 adsorption-desorption equilibrium is included (R3 in Table 1). Photogeneration of charge carriers, electron-hole pairs, take place via absorption of light by the photocatalyst (R1 in Table 1). The photogenerated holes could have three plausible destinations:

- (i) recombination with photogenerated electrons (R2 in Table 1),
- (ii) trapping by water molecules and hydroxide ions leading to hydroxyl radicals formation (R6 and R7 in Table 1),
- (iii) trapping by BR46 molecules and BR46 degradation intermediates (R8 and R9 in Table 1).

By considering the synergetic role between hydroxyl radicals and holes in photocatalytic degradation of the BR46, the overall reaction rate ($r_{Overall}$) could be expressed as Eq. (2):

$$\frac{-dC_{BR46}}{dt} = k_{BR46} [h^+] [BR46]_{ads} + k_{\cdot OH, BR46} [\cdot OH]_{ads} [BR46]_{ads} \quad (2)$$

where C_{BR46} is the concentration of BR46 at time t , k_{BR46} is the rate constant of direct oxidation of BR46 on photogenerated holes and $k_{\cdot OH, BR46}$ is the rate constant for reaction between adsorbed hydroxyl radicals ($[\cdot OH]_{ads}$) and BR46 molecules ($[BR46]_{ads}$). The overall reaction rate contains two unstable reactive species; i.e. hydroxyl radicals and photogenerated holes, whose concentration could be calculated by the steady-state approximation (SSA). By considering the steady state concentration between t and $t+dt$, concentration of $[\cdot OH]_{ads}$ could be expressed as:

$$\frac{d[\cdot OH]_{ads}}{dt} = k_{H_2O} [h^+] [H_2O]_{ads} + k_{OH^-} [h^+] [OH^-]_{ads} - k_{\cdot OH, Int} [\cdot OH]_{ads} [Int]_{ads} - k_{inact} [\cdot OH]_{ads} = 0 \quad (3)$$

We reasonably assumed that the hydroxyl radicals are mainly formed via trapping of the photogenerated holes by water molecules because water is the solvent. In our experiments, the moles of water and hydroxide ions were 11.11 and 2×10^{-6} , respectively. Accordingly, the equilibrium of adsorption reaction (R4 in

$$\frac{d[\cdot OH]_{ads}}{dt} = k_{H_2O} [h^+] [H_2O]_{ads} + k_{OH^-} [h^+] [OH^-]_{ads} - k_{\cdot OH, Int} [\cdot OH]_{ads} [Int]_{ads} - k_{inact} [\cdot OH]_{ads} = 0 \quad (3)$$

band gap energy of ZS. In the second mechanism, CNT could be considered as the macromolecular photosensitizer [15]. In this regard, the excitation of the CNT takes place by light photons to triplet

Table 1) lies far to the right and $[H_2O]_{ads}$ remains relatively constant in aqueous media. By defining $k_{H_2O}[H_2O]_{ads} = k'_{H_2O}$:

$$[\cdot OH]_{ads} = \frac{k'_{H_2O}[h^+]}{k_{\cdot OH, BR46}[BR46]_{ads} + k_{\cdot OH, Int}[Int]_{ads} + k_{inact}} \quad (4)$$

In Eq. (4), it is difficult to measure $[BR46]_{ads}$ and $[Int]_{ads}$, greatly. So, the following assumption was considered:

$$[BR46]_0 = [BR46]_{aq} + [BR46]_{ads} + [Int]_{ads} \Rightarrow [BR46]_0$$

$$= \frac{K_{BR46} + 1}{K_{BR46}} [BR46]_{ads} + [Int]_{ads} \quad (5)$$

where K_{BR46} is linear BR46 liquid–solid adsorption equilibrium constant (L/g).

$$\begin{aligned} k_{\cdot OH, BR46}[BR46]_{ads} + k_{\cdot OH, Int}[Int]_{ads} &= \frac{k_{\cdot OH, BR46}K_{BR46}}{K_{BR46} + 1} ([BR46]_0 - [Int]_{ads}) + \\ k_{\cdot OH, Int}([BR46]_0 - \frac{K_{BR46} + 1}{K_{BR46}} [BR46]_{ads}) &= (\frac{k_{\cdot OH, BR46}K_{BR46}}{K_{BR46} + 1} + k_{\cdot OH, Int}) [BR46]_0 - \\ \frac{k_{\cdot OH, BR46}K_{BR46}}{K_{BR46} + 1} [Int]_{ads} - \frac{k_{\cdot OH, Int}(K_{BR46} + 1)}{K_{BR46}} [BR46]_{ads} &\approx (\frac{k_{\cdot OH, BR46}K_{BR46}}{K_{BR46} + 1} + k_{\cdot OH, Int}) [BR46]_0 \end{aligned} \quad (6)$$

In Eq. (6), it has been assumed that $(\frac{k_{\cdot OH, BR46}K_{BR46}}{K_{BR46} + 1} + k_{\cdot OH, Int}) [BR46]_0$ is higher than $[BR46]_{ads} \frac{k_{\cdot OH, BR46}K_{BR46}}{K_{BR46} + 1} [Int]_{ads}$ and $\frac{k_{\cdot OH, Int}(K_{BR46} + 1)}{K_{BR46}} [BR46]_{ads}$.

By applying the mentioned assumption, Eq. (4) could be modified as:

$$[\cdot OH]_{ads} = \frac{\frac{k'_{H_2O}}{k_{inact}} [h^+]}{1 + \left(\frac{k_{\cdot OH, BR46}K_{BR46}}{(K_{BR46} + 1)(k_{inact})} + \frac{k_{\cdot OH, Int}}{k_{inact}} \right) [BR46]_0} \quad (7)$$

During dt , the steady state equation for holes:

$$\begin{aligned} \frac{d[h^+]}{dt} &= k_{irr}I + k_{inact} [\cdot OH] - (k_{recomb} [h^+] [e^-] + k_{H_2O} [h^+] [H_2O]_{ads} + k_{OH^-} [h^+] [OH^-]_{ads} + k_{BR46} [h^+] [BR46]_{ads} \\ &+ k_{Int} [h^+] [Int]_{ads}) = 0 \end{aligned} \quad (8)$$

Because the photocatalyst particles are electrically neutral, the concentration of $[h^+]$ and $[e^-]$ is equated. The assumption 4 was inserted in Eq. (9) to obtain the equation with measurable parameters:

$$\begin{aligned} k_{irr}I + k_{inact} [\cdot OH] - (k_{recomb} [h^+]^2 + k_{H_2O} [h^+] [H_2O]_{ads} \\ + k_{OH^-} [h^+] [OH^-]_{ads} + (\frac{k_{BR46}K_{BR46}}{K_{BR46} + 1} + k_{Int}) [h^+] [BR46]_0) = 0 \end{aligned} \quad (9)$$

then, it was fitted on experimental initial rates. Firstly, the Eq. (2) was rearranged as Eq. (13):

$$r_{Overall} = \frac{-dC_{BR46}}{dt} = \left(K_{BR46}k_{BR46}[h^+] + K_{BR46}k_{OH, BR46} [\cdot OH]_{ads} \right) [BR46]_{aq} \quad (13)$$

Then, Eq. (12) was substituted in Eq. (7) and then (13). With assuming extreme case in which water molecules is the main trapping agent of photogenerated holes, the photocatalytic degradation rate ($r_{Overall(WT)}$) for BR46 on ZSC was achieved as:

$$r_{Overall} = \frac{\left(\frac{k_{irr}k_{BR46}K_{BR46}}{k'_{H_2O}} + \frac{k_{irr}k_{OH, BR46}K_{BR46}}{k_{inact}} \right) I + \left(\frac{k_{irr}k_{\cdot OH, BR46}K_{BR46}^2}{(K_{BR46} + 1)k_{inact}k'_{H_2O}} + \frac{k_{irr}k_{\cdot OH, Int}k_{BR46}K_{BR46}}{k_{inact}k'_{H_2O}} \right) I[BR46]_0}{1 + \left(\frac{k_{\cdot OH, BR46}K_{BR46}}{(K_{BR46} + 1)(k_{inact})} + \frac{k_{\cdot OH, Int}}{k_{inact}} \right) [BR46]_0} [BR46]_{aq} \quad (14)$$

By considering the $k_{H_2O} [h^+] [H_2O]_{ads} \gg k_{OH^-} [h^+] [OH^-]_{ads}$ and $k_{H_2O} [H_2O]_{ads} = k'_{H_2O}$.

$$k_{irr}I + k_{inact} [\cdot OH] - \left(k_{recomb} [h^+]^2 + k'_{H_2O} [h^+] + \left(\frac{k_{BR46}K_{BR46}}{K_{BR46} + 1} + k_{Int} \right) [h^+] [BR46]_0 \right) = 0 \quad (10)$$

Herein, the hole trapping by water or BR46 molecules could completely compete with free carrier recombination

because PL signal decreases significantly in ZS after the combination with CNT indicating the depression of the electron-hole recombination. In other words, we assumed: $k'_{H_2O} [h^+] + \left(\frac{k_{BR46}K_{BR46}}{K_{BR46} + 1} + k_{Int} \right) [h^+] [BR46]_0 \gg k_{recomb} [h^+]^2$. On the other hand, experimental results showed that initial photocatalytic degradation rate depend on light intensity with first-order kinetic as intensity increases. Since R12 is exclusively one path for inactivation of the hydroxyl radicals, it is clear that $k_{irr}I \gg k_{inact} [\cdot OH]$. Taking into account the mentioned reasons, Eq. (8) will be simplified to:

$$[h^+] = \frac{k_{irr}I}{k'_{H_2O} + \left(\frac{k_{BR46}K_{BR46}}{K_{BR46} + 1} + k_{Int} \right) [BR46]_0} \quad (11)$$

An extreme case of Eq. (11) is when $k'_{H_2O} \geq \left(\frac{k_{BR46}K_{BR46}}{K_{BR46} + 1} + k_{Int} \right) [BR46]_0$. Because, at the beginning of reaction the moles of water and BR46 were about 11.11 and 3×10^{-6} , respectively. Consequently:

$$[h^+] = \frac{k_{irr}I}{k'_{H_2O}} \quad (12)$$

By considering the mentioned extreme case (Eq. (12)), a rate equation was developed for photocatalytic degradation of BR46 and

then, it was fitted on experimental initial rates. Firstly, the Eq. (2) was rearranged as Eq. (13):

$$r_{Overall} = \frac{-dC_{BR46}}{dt} = \left(K_{BR46}k_{BR46}[h^+] + K_{BR46}k_{OH, BR46} [\cdot OH]_{ads} \right) [BR46]_{aq} \quad (13)$$

Then, Eq. (12) was substituted in Eq. (7) and then (13). With assuming extreme case in which water molecules is the main trapping agent of photogenerated holes, the photocatalytic degradation rate ($r_{Overall(WT)}$) for BR46 on ZSC was achieved as:

This equation has three adjustable parameters: $\frac{k_{irr}k_{BR46}K_{BR46}}{k'_{H_2O}} +$

Table 2
Values of adjustable parameters.

Rate equation	Adjustable constant	Value	R ²	RMSE
$r_{Overall} = \frac{\alpha I + \beta I[BR46]_0}{1 + \gamma [BR46]_0} [BR46]_{aq}$	$\alpha = \frac{k_{irr} k_{OH, BR46} K_{BR46}}{k'_{H_2O}} + \frac{k_{irr} k_{OH, BR46} K_{BR46}}{k_{inact}}$	3.9×10^{-4}	0.990	7.12×10^{-4}
	$\beta = \frac{k_{irr} k_{OH, BR46} k_{BR46} K_{BR46}^2}{(K_{BR46} + 1) k_{inact} k'_{H_2O}} + \frac{k_{irr} k_{OH, Int} k_{BR46} K_{BR46}}{k_{inact} k'_{H_2O}}$	-2.4×10^{-5}		
	$\gamma = \frac{k_{OH, BR46} K_{BR46}}{(K_{BR46} + 1)(k_{inact})} + \frac{k_{OH, Int}}{k_{inact}}$	-6.6×10^{-2}		

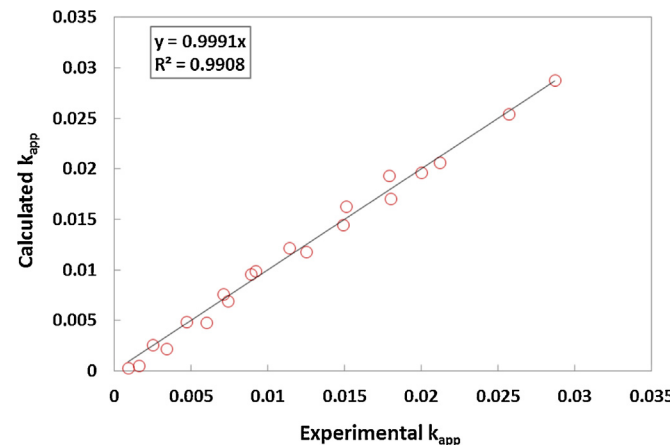


Fig. 7. Comparison of the experimental rate constant with those calculated via developed kinetic model (Eq. (16)).

$$\frac{k_{irr} k_{OH, BR46} K_{BR46}}{k_{inact}}, \quad \frac{k_{irr} k_{OH, BR46} k_{BR46} K_{BR46}^2}{(K_{BR46} + 1) k_{inact} k'_{H_2O}} + \frac{k_{irr} k_{OH, Int} k_{BR46} K_{BR46}}{k_{inact} k'_{H_2O}}$$

and $\frac{k_{OH, BR46} K_{BR46}}{(K_{BR46} + 1)(k_{inact})} + \frac{k_{OH, Int}}{k_{inact}}$. The Eq. (14) could be simplified to Eq. (15):

$$r_{Overall} = \frac{\alpha I + \beta I[BR46]_0}{1 + \gamma [BR46]_0} [BR46]_{aq} \quad (15)$$

In fact, this equation suggests a first order kinetics for photocatalytic degradation of BR46 with considering the steady state concentration for the main oxidizing species including photogenerated holes and hydroxyl radicals, i.e.:

$$k_{apparent, cal.} = \frac{\left(\frac{k_{irr} k_{BR46} K_{BR46}}{k'_{H_2O}} + \frac{k_{irr} k_{OH, BR46} K_{BR46}}{k_{inact}} \right) I + \left(\frac{k_{irr} k_{OH, BR46} k_{BR46} K_{BR46}^2}{(K_{BR46} + 1) k_{inact} k'_{H_2O}} + \frac{k_{irr} k_{OH, Int} k_{BR46} K_{BR46}}{k_{inact} k'_{H_2O}} \right) I[BR46]_0}{1 + \left(\frac{k_{OH, BR46} K_{BR46}}{(K_{BR46} + 1)(k_{inact})} + \frac{k_{OH, Int}}{k_{inact}} \right) [BR46]_0} \quad (16)$$

This equation explain the interdependence of the apparent rate constant ($k_{apparent}$) with the effective operational parameters on process rate. The adjustable parameters including α , β and γ were calculated by linear least square method using Matlab 7.9.0 software. The apparent rate constants calculated based on a correct rate equation would be most consistent with experimental data. Consequently, the obtained adjustable parameters were inserted in Eq. (16), and the apparent rate constants ($k_{apparent, cal.}$) were calculated in different conditions. To evaluate the obtained rate equation, the calculated apparent rate constants were compared with experimental ones and then, correlation coefficients (R^2) root-mean-square-error (RMSE) were calculated. Based on the results given in Fig. 7 Table 2, the calculated apparent rate constants are in excellent agreement with experimental $k_{apparent}$. The experimental and calculated initial photocatalytic degradation rates (using Eq. (15)) in different operational conditions has been also shown in Fig. 8. It is clear that the developed rate equation describes the experimental results adequately. This excellent fit obtained for photocatalytic degradation of BR46 on ZSC implies that the

rate equation was developed based on the reliable and reasonable mechanism and assumptions.

The results presented in Fig. 8a indicated that the photocatalytic degradation rate increased with the increase in BR46 initial concentration to 14 mg/L. A further increase in initial concentration led to decrease in photocatalytic degradation rate. Also, the photocatalytic degradation rate increased with the increase in light intensity (Fig. 8b). The rate of photocatalytic degradation depends on two factors: (i) probability of holes photogeneration and •OH radicals formation and (ii) probability of photogenerated holes and •OH radicals reaction with BR46 molecules. As the initial BR46 concentration increase, the number of effective collisions in unit of time between BR46 molecules and oxidizing species also increases, leading to photocatalytic degradation rate enhancement. On the contrary, at high BR46 concentration, the generation of the holes and •OH radicals suppress due to occupying the catalyst surface and/or light-screening effect of the dye.

3.3. Byproducts of BR46 photocatalytic degradation on ZSC

In the last part of our research work, final byproducts of BR46 photocatalysis on ZSC were identified by GC-MS analysis. The photocatalytic of BR46 was carried out by ZSC (140 mg/L) on solution containing 20 mg/L of BR46 at pH equal to 9 during 120 min of irradiation. The photocatalytic experiment was repeated three times and the formed byproducts were extracted by 30 mL of diethyl ether. By analyzing the main fragments of mass spectra, we could identify six byproducts. However, there were some peaks in GC which not recognized from their mass spectra due to the limitations analytical technique or lack of significant accumulation of byproduct in the organic medium. The identified products, the related

main fragments of mass spectra and retention time (t_R) are given in Table 3.

4. Conclusion

In summary, we have synthesized the ZSC nanocomposite by a facile two-step process. It has been showed that the as-prepared ZSC nanocomposite can be used as an efficient photocatalyst to degrade organic dyes. The studies indicate that the ZSC nanocomposite shows much higher photocatalytic activity in comparison with bare ZS. Furthermore, the possible role of the MWCNTs on of photoactivity of nanocomposite was investigated using appropriate radical scavengers. It has been found that the major oxidative splices in this process was h^+ as the addition of KI inhabited completely the photocatalytic degradation of RB46. It is also revealed from DRS and PL spectra that ZSC nanocomposite exhibited narrower band gap and weaker PL emission intensity than that of

Table 3

Possible byproducts identified as degradation products of RB19 photocatalytic degradation, Operational conditions: [ZSC] = 140 mg/L, [BR46] = 20 mg/L, Time = 120 min, pH = 9 and L.I. = 36 W/m².

Peak of Chromathogram	Retention time (min)	Main fragments	Proposed structure	IUPAC name
A	7.62	113, 87, 85, 57, 42, 27		2,4-dimethyl-2H-1,2,4-triazol-3(4H)-one
B	4.65	154, 137, 126, 109, 108, 71, 45		3-hydroxybenzoic acid (It is also meta or para substitution)
C	5.21	109, 92, 66, 80, 53, 28		4-aminophenol
D	5.980	110, 81, 74, 52		Hydroquinone
E	3.80	94, 66, 39, 28		Phenol
F	4.12	116, 99, 72, 60, 54, 45, 17		Maleic acid

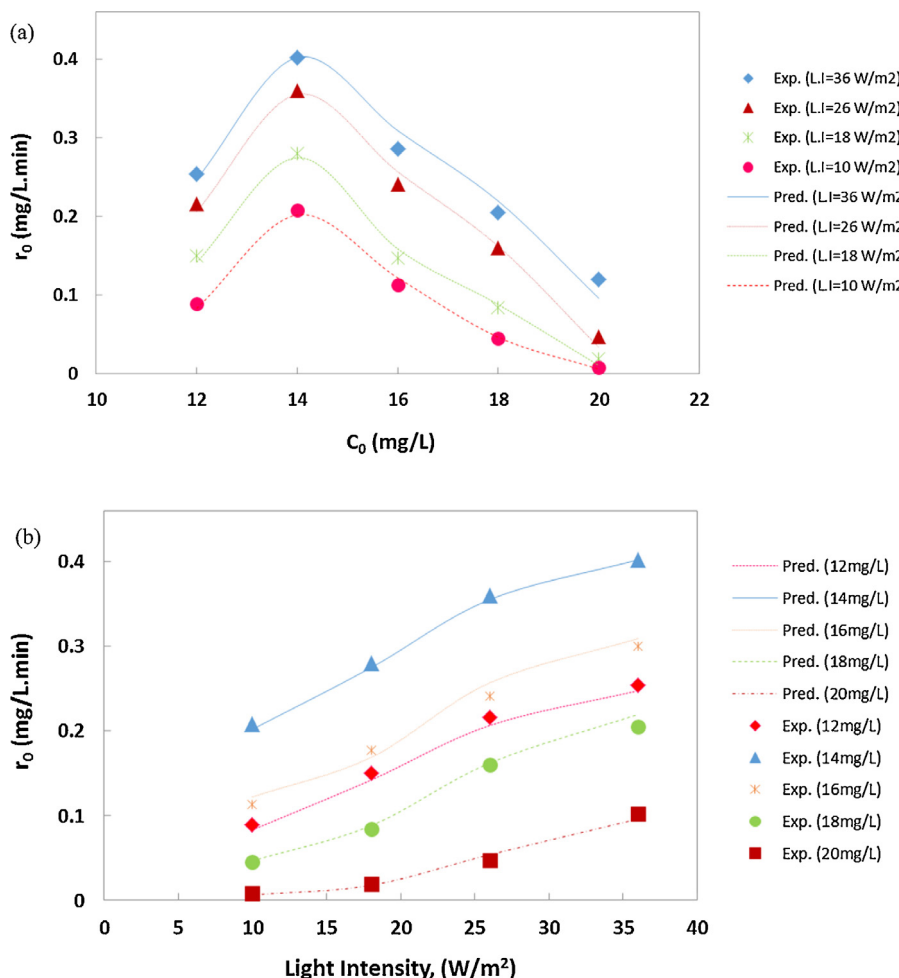


Fig. 8. Calculated initial photocatalytic degradation rate r_0 as a function of (a) initial BR46 concentration ($L \cdot I = 36 \text{ W/m}^2$) and (b) light intensity ($[BR46] = 14 \text{ mg/L}$).

ZS. From the results of experiments and DRS and PL spectra, it can be suggested that narrow band gap MWCNTs get excited by absorbing the irradiated photons, generating electron-hole pairs on the CNTs. The photogenerated electrons then transfer to CB of the ZS and the positively charged CNT remove an electron from the VB of the ZS. The formed holes on the VB of ZS then can react with dye and/or water molecules to generate the hydroxyl radicals. Moreover, a kinetic model was developed based on the intrinsic elementary reactions and the proposed mechanism. The good agreement between the calculated apparent rate constants and experimental ones confirms the proposed mechanism and indicates that the rate equation was developed based on the reliable and reasonable mechanism and assumptions.

References

- [1] V. Georgakilas, J.A. Perman, J. Tucek, R. Zboril, Broad family of carbon nanoallotropes: classification, chemistry, and applications of fullerenes, carbon dots, nanotubes, graphene, nanodiamonds, and combined superstructures, *Chem. Rev.* 115 (11) (2015) 4744–4822.
- [2] M. Engel, J.P. Small, M. Steiner, M. Freitag, A.A. Green, M.C. Hersam, P. Avouris, Thin film nanotube transistors based on self-assembled aligned, semiconducting carbon nanotube arrays, *ACS Nano* 2 (2008) 2445–2452.
- [3] P. Ma, Q. Zheng, E. Mäder, J. Kim, Behavior of load transfer in functionalized carbon nanotube/epoxy nanocomposites, *Polymer (Guildf)* 53 (2012) 6081–6088.
- [4] Z. Wen, S. Ci, S. Mao, S. Cui, Z. He, J. Chen, CNT @ TiO₂ nanohybrids for high-performance anode of lithium-ion batteries, *Nanoscale Res. Lett.* 8 (1) (2013) 1–6.
- [5] W.J. Lee, J.M. Lee, S.T. Kochuveedu, T.H. Han, H.Y. Jeong, M. Park, J.M. Yun, J. Kwon, K. No, D.H. Kim, S.O. Kim, Biominerilized N-doped CNT/TiO₂ core/shell nanowires for visible light photocatalysis, *ACS Nano* 6 (1) (2011) 935–943.
- [6] B.K. Vijayan, N.M. Dimitrijevic, D. Finkelstein-shapiro, J. Wu, K.A. Gray, Coupling titania nanotubes and carbon nanotubes to create photocatalytic nanocomposites, *ACS Catal.* 2 (2) (2012) 223–229.
- [7] K.E. Tettey, M.Q. Yee, D. Lee, Photocatalytic and conductive MWNT/TiO₂ nanocomposite thin films, *ACS Appl. Mater. Interfaces* 2 (2010) 2646–2652.
- [8] Y. Yan, J. Miao, Z. Yang, F.X. Xiao, H.B. Yang, B. Liu, Y. Yang, Carbon nanotube catalysts: recent advances in synthesis, characterization and applications, *Chem. Soc. Rev.* 44 (10) (2015) 3295–3346.
- [9] R. Leary, A. Westwood, Carbonaceous nanomaterials for the enhancement of TiO₂ photocatalysis, *Carbon N. Y.* 49 (2011) 741–772.
- [10] K. Woan, G. Pyrgiotakis, W. Sigmund, Photocatalytic carbon-nanotube-TiO₂ composites, *Adv. Mater.* 21 (2009) 2233–2239.
- [11] W. Chen, Z. Fan, B. Zhang, K. Takanabe, X. Zhang, Z. Lai, Enhanced visible-light activity of titania via confinement inside carbon nanotubes, *J. Am. Chem. Soc.* 133 (38) (2011) 14896–14899.
- [12] Y. Xu, Y. Zhuang, X. Fu, New insight for enhanced photocatalytic activity of TiO₂ by doping carbon nanotubes: a case study on degradation of benzene and methyl orange, *J. Phys. Chem. C* 114 (6) (2010) 2669–2676.
- [13] K. Zhang, F.J. Zhang, M.L. Chen, W.C. Oh, Comparison of catalytic activities for photocatalytic and sonocatalytic degradation of methylene blue in present of anatase TiO₂-CNT catalysts, *Ultrason. Sonochem.* 18 (2011) 765–772.
- [14] Y. Zhang, Z.R. Tang, X. Fu, Y.J. Xu, TiO₂-graphene nanocomposites for gas-phase photocatalytic degradation of volatile aromatic pollutant: is TiO₂-graphene truly different from other TiO₂-carbon composite materials? *ACS Nano* 4 (2010) 7303–7314.
- [15] Y. Zhang, N. Zhang, Z.R. Tang, Y.J. Xu, Graphene transforms wide band gap ZnS to a visible light photocatalyst. The new role of graphene as a macromolecular photosensitizer, *ACS Nano* 6 (11) (2012) 9777–9789.
- [16] W. Wang, P. Serp, P. Kalck, J. Lu, Visible light photodegradation of phenol on MWNT-TiO₂ composite catalysts prepared by a modified sol-gel method, *J. Mol. Catal. A* 235 (2005) 194–199.
- [17] B.K. Woan, G. Pyrgiotakis, W. Sigmund, Photocatalytic carbon-nanotube-TiO₂ composites, *Adv. Mater.* 21 (21) (2009) 2233–2239.

[18] G. Pyrgiotakis, S. Lee, W. Sigmund, Advanced photocatalysis with anatase nano-coated multi-walled carbon nanotubes, *Mater. Res.* 876 (2005) 1–6.

[19] Y. Yu, J.C. Yu, C.Y. Chan, Y.K. Che, J.C. Zhao, L. Ding, W.K. Ge, P.K. Wong, Enhancement of adsorption and photocatalytic activity of TiO₂ by using carbon nanotubes for the treatment of azo dye, *Appl. Catal. B Environ.* 61 (2005) 1–11.

[20] Y. Yao, G. Li, S. Ciston, R.M. Lueptow, K.A. Gray, Photoreactive TiO₂/carbon nanotube composites: synthesis and reactivity, *Environ. Sci. Technol.* 42 (2008) 4952–4957.

[21] H. Wang, D. Xie, Q. Chen, C. You, Kinetic modeling for the deactivation of TiO₂ during the photocatalytic removal of low concentration SO₂, *Chem. Eng. J.* 303 (2016) 425–432.

[22] M.H. Rasoulifard, M.S.S. Dorraji, S. Taherkhani, Photocatalytic activity of zinc stannate: preparation and modeling, *J. Taiwan Inst. Chem. Eng.* 58 (2016) 324–332.

[23] A.R. Amani-Ghadim, M.S.S. Dorraji, Modeling of photocatalytic process on synthesized ZnO nanoparticles: kinetic model development and artificial neural networks, *Appl. Catal. B Environ.* 163 (2015) 539–546.

[24] H.Q. Wu, Q.Y. Wang, Y.Z. Yao, C. Qian, X.J. Zhang, X.W. Wei, Microwave-assisted synthesis and photocatalytic properties of carbon nanotube/zinc sulfide heterostructures, *J. Phys. Chem. C* 112 (2008) 16779–16783.

[25] B. Weng, S. Liu, N. Zhang, Z.R. Tang, Y.J. Xu, A simple yet efficient visible-light-driven CdS nanowires-carbon nanotube 1D-1D nanocomposite photocatalyst, *J. Catal.* 309 (2014) 146–155.

[26] T. Lv, L. Pan, X. Liu, T. Lu, G. Zhu, Z. Sun, Enhanced photocatalytic degradation of methylene blue by ZnO-reduced graphene oxide composite synthesized via microwave-assisted reaction, *J. Alloys Compd.* 509 (2011) 10086–10091.

[27] J. Yu, B. Yang, B. Cheng, Noble-metal-free carbon nanotube-Cd0.1Zn0.9S composites for high visible-light photocatalytic H₂-production performance, *Nanoscale* 4 (8) (2012) 2670–2677.

[28] K. Dai, G. Dawson, S. Yang, Z. Chen, L. Lu, Large scale preparing carbon nanotube/zinc oxide hybrid and its application for highly reusable photocatalyst, *Chem. Eng. J.* 191 (2012) 571–578.

[29] D. Chen, J. Xu, B. Liang, X. Wang, P.-C. Chen, C. Zhou, G. Shen, Electric transport, reversible wettability and chemical sensing of single-crystalline zigzag Zn₂SnO₄ nanowires, *J. Mater. Chem.* 21 (2011) 17236–17241.

[30] B. Tan, E. Toman, Y. Li, Y. Wu, Zinc stannate (Zn₂SnO₄) dye-sensitized solar cells, *J. Am. Chem. Soc.* 129 (14) (2007) 4162–4163.

[31] C. Yan, J. Yang, Q. Xie, Z. Lu, B. Liu, C. Xie, S. Wu, Y. Zhang, Y. Guan, Novel nanoarchitected Zn₂SnO₄ anchored on porous carbon as high performance anodes for lithium ion batteries, *Mater. Lett.* 138 (2015) 120–123.

[32] L. Shi, Y. Dai, Synthesis and photocatalytic activity of Zn₂SnO₄ nanotube arrays, *J. Mater. Chem. A* 1 (2013) 12981–12986.

[33] S. Danwittayakul, M. Jaisai, T. Koottatep, J. Dutta, Enhancement of photocatalytic degradation of methyl orange by supported zinc oxide nanorods/zinc stannate (ZnO/ZTO) on porous substrates, *Ind. Eng. Chem. Res.* 52 (2013) 13629–13636.

[34] Y. Zhao, L. Hu, H. Liu, M. Liao, X. Fang, L. Wu, Band gap tunable Zn₂SnO₄ nanocubes through thermal effect and their outstanding ultraviolet light photoresponse, *Sci. Rep.* 4 (2014).

[35] M. Ben Ali, H.H. Yolcu, H. Elhouichet, B. Sieber, A. Addad, L. Boussekey, M. Moreau, M. Férid, S. Szunerits, R. Boukherroub, Hydrothermal synthesis of ZTO/graphene nanocomposite with excellent photocatalytic activity under visible light irradiation, *J. Colloid Interface Sci.* 473 (2016) 66–74.

[36] Z.Z. Jiang, Z.B. Wang, Y.Y. Chu, D.M. Gu, G.P. Yin, Carbon riveted microcapsule Pt/MWCNTs-TiO₂ catalyst prepared by in situ carbonized glucose with ultrahigh stability for proton exchange membrane fuel cell, *Energy Environ. Sci.* 4 (7) (2011) 2558–2566.

[37] J.M. Chem, A.M. Baker, L. Wang, S.G. Advani, A.K. Prasad, Nafion membranes reinforced with magnetically controlled Fe₃O₄-MWCNTs for PEMFCs, *J. Mater. Chem.* 22 (28) (2012) 14008–14012.

[38] H. Zhang, M. Bayne, S. Fernando, B. Legg, M. Zhu, R.L. Penn, J.F. Ban, Size-dependent bandgap of nanogoeite, *J. Phys. Chem. C* 115 (36) (2011) 17704–17710.

[39] M.A. Alpuche-aviles, Y. Wu, M.A. Alpuche-aviles, Y. Wu, Photoelectrochemical study of the band structure of Zn SnO prepared by the hydrothermal method photoelectrochemical study of the band structure of Zn₂SnO₄ prepared by the hydrothermal method, *J. Am. Chem. Soc.* 131 (9) (2009) 3216–3224.

[40] I. Robel, B.A. Bunker, P.V. Kamat, Single-walled carbon nanotube-CdS nanocomposites as light-harvesting assemblies: photoinduced charge-transfer interactions, *Adv. Mater.* 17 (2005) 2458–2463.